

Development of a compact magnetic resonance imaging system for a cold room

Satoru Adachi,¹ Toshihiro Ozeki,² Ryosuke Shigeki,¹ Shinya Handa,¹ Katsumi Kose,^{1,a)} Tomoyuki Haishi,³ and Masaaki Aoki⁴

¹*Institute of Applied Physics, University of Tsukuba, Tsukuba, Ibaraki 305-8573, Japan*

²*Hokkaido University of Education, Sapporo, Hokkaido 002-8502, Japan*

³*MRTechnology Inc., Tsukuba, Ibaraki 305-0047, Japan*

⁴*Hitachi Metals Co. Ltd., Omachi, Saga 849-2102, Japan*

(Received 25 December 2008; accepted 14 April 2009; published online 7 May 2009)

A compact magnetic resonance imaging (MRI) system for a cold ($-5\text{ }^{\circ}\text{C}$) room has been developed to acquire MR images below the freezing point of water. The MRI system consists of a 1.0 T permanent magnet, a higher-order shim coil set, and a gradient coil probe, installed in the cold room, and a compact MRI console installed in a room at normal temperature ($20\text{--}25\text{ }^{\circ}\text{C}$). The most difficult problem for the installation of the MRI system in the cold room was the degradation of the field homogeneity of the permanent magnet shimmed at $25\text{ }^{\circ}\text{C}$. To overcome this problem, higher-order shim coils were developed and the temperature variation of the magnetic field distribution was measured using a standard phantom with and without shim coil currents. As a result, it was confirmed that the homogeneity (the difference between the minimum and maximum values) of the magnetic field in the $17\times 17\times 19\text{ mm}^3$ rectangular parallelepiped region was improved from 117 to 59 ppm using an appropriate combination of shim coil currents. A snowpack immersed in dodecane ($\text{C}_{12}\text{H}_{26}$) was imaged using a driven-equilibrium three-dimensional (3D) spin-echo sequence at $-5\text{ }^{\circ}\text{C}$. The visualized 3D structure of the snowpack demonstrated the effectiveness of our approach. © 2009 American Institute of Physics. [DOI: 10.1063/1.3129362]

I. INTRODUCTION

Magnetic resonance imaging (MRI) systems using permanent magnets have several advantages over those using superconducting magnets. The first is portability; this is because the permanent magnets do not need a cryostat or a power source. The second is openness, or accessibility to the sample; this is because the superconducting magnets of the normal design have a long cylindrical bore.

There are, of course, several drawbacks in using permanent magnets rather than superconducting magnets in MRI. The first is a limitation on the magnetic field strength. The highest magnetic field ever reported for permanent magnets for MRI is 2.0 T,¹ much lower than for superconducting magnets [17.6 T ,^{2,3} 18.8 T (Ref. 4)] for MRI. The second is the temperature drift of the magnetic field, an effect caused by the relatively large temperature coefficients of residual magnetic flux density of the permanent magnet materials.⁵ The temperature drift, however, can be overcome by a combination of magnet temperature control and a NMR lock technique.⁶

The portability of MRI systems using the permanent magnets can extend the possibility of MRI applications. In this work, we have developed a compact MRI system using a permanent magnet for a cold ($-5\text{ }^{\circ}\text{C}$) room to perform several useful MRI applications below the freezing point of wa-

ter. To the best of our knowledge, this is the first MRI system constructed in the low temperature environment.

II. THE COMPACT MRI SYSTEM

The compact MRI system consisted of a permanent magnet, a higher-order shim coil set, a gradient coil probe, and a compact MRI console. The magnet, shim coil set, and gradient probe were installed in a cold room (4.8 m wide, 2.4 m high, and 2.5 m long) and the MRI console was installed in a room at normal temperature ($20\text{--}25\text{ }^{\circ}\text{C}$), next to the cold room. The temperature of the cold room can be kept at any temperature between -5 and $10\text{ }^{\circ}\text{C}$. The control or signal lines for the shim coils, gradient coils, and rf coil were connected to the MRI console through a hole opened in the wall between the cold room and the operation room. Figure 1 shows an overview of the MRI detection system installed in the cold room.

The magnet (Hitachi Metals Co., Omachi, Saga, Japan, $481\times 352\times 352\text{ mm}^3$, 350 kg) had a yokeless design⁷⁻¹⁰ and consisted of NdFeB (Ref. 11) material blocks. The field strength was 1.0 T, the gap width was 60 mm, and the homogeneity was 15.3 ppm over 30 mm diameter spherical volume. The homogeneity of the magnet was carefully adjusted with a passive shim technique using pieces of permanent magnets in a temperature-regulated room ($25\text{ }^{\circ}\text{C}$) in the factory.¹²

The higher-order planar shim coils were designed according to Anderson's approach.¹³ The spatial distributions of the magnetic field produced by the shim coils were pro-

^{a)} Author to whom correspondence should be addressed. Electronic mail: kose@bk.tsukuba.ac.jp.



FIG. 1. (Color online) MRI detection system installed in the cold ($-5\text{ }^{\circ}\text{C}$) room. The system consists of a permanent magnet, a higher-order shim coil set, and a gradient probe. The shim coil set and gradient probe are connected to the MRI console installed in the adjacent operation room.

portional to xy , x^2-y^2 , z^2 , and z^3 . The coils were wound on Bakelite plates using polyethylene-coated Cu wire (1.0 mm diameter) and fixed with epoxy resin. The shim coils were driven with constant current power sources.

The planar gradient coils were designed in the following way. The x and y coils were designed using the target field method¹⁴ modified for the planar coil,¹⁵ and the z -gradient coil was designed as a combination of circular current loops with diameters optimized using the genetic algorithm.¹⁶ Figure 2 shows the wire pattern for the x - or y -, and z -gradient coils.

The gradient coil elements (x , y , and z) were wound on a fiber reinforced plastic square plate ($0.5 \times 140 \times 140\text{ mm}^3$) using a 0.5 mm diameter polyethylene-coated Cu wire. After the coil wires were fixed using epoxy resin, the x , y , and z coil elements were stacked together and fixed using epoxy resin. Two sets of the stacked elements were fixed parallel to each other on both sides of a rf shield box ($38.6 \times 140 \times 140\text{ mm}^3$) made of a square aluminum frame (38 mm wide, 6.0 mm thick) and two 0.3 mm thick brass side plates. The Cu wires of the two coil elements were connected together and driven by gradient drivers ($\pm 10\text{ A}$). The efficiency of the gradient coils were 30.3, 29.0, and 57.9 mT/mA for the x -, y -, and z -gradient coils, respectively.

The RF coil was a 10-turn solenoid wound on an acrylic pipe (30 mm outer diameter, 26 mm inner diameter) using a polyethylene-coated Cu wire of 2.0 mm diameter and placed at the center of the rf shield box. The solenoid coil was tuned to the NMR resonance frequency (44.12 MHz) and matched to $50\text{ }\Omega$ using three variable capacitors (NMAP40HV, Vol-

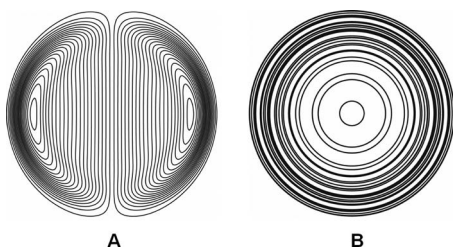


FIG. 2. (a) Current pattern for the x - or y -gradient coil. This pattern was calculated using the target field method. (b) Current pattern for the z -gradient coil. This pattern was calculated using the genetic algorithm.

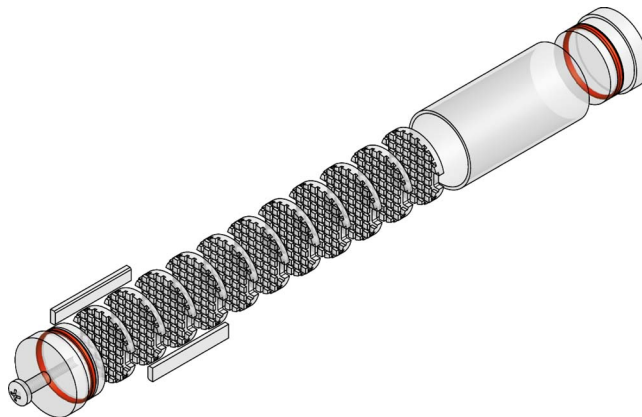


FIG. 3. (Color online) Structure of the standard phantom. The outer and inner diameters of the cylindrical container are 26 and 24 mm, respectively.

tronics Corp., Denville, USA). The rf probe box was fixed in the gap space of the magnet, and the rf coil and the gradient coils were connected to the MRI console.

The MRI console consists of an industrial PC, a MRI transceiver (MRTechnology, Tsukuba, Japan), a transmitter driver (DS Technology, Asaka, Japan), and a three-channel gradient driver (Jyonan Electric Laboratory, Tsukuba, Japan). The details of the MRI console are described elsewhere.¹⁷

III. EXPERIMENTS

The variation of the magnetic field distribution with temperature was measured using a standard phantom consisting of 3 mm thick circular (23.9 mm diameter) plastic disks with grid-shaped trenches (3 mm pitch, 1 mm depth) stacked in a cylindrical plastic container (24 mm inner diameter, 61 mm length) filled with baby oil (Johnson & Johnson, USA). The baby oil was used because it does not freeze even at $-5\text{ }^{\circ}\text{C}$. The structure of the phantom is shown in Fig. 3.

MR images of the phantom were acquired with a three-dimensional (3D) driven-equilibrium spin-echo sequence (repetition time=200 ms, echo time=8 ms, number of excitation=4, image matrix= 256^3 , voxel size= $(100\text{ }\mu\text{m})^3$) at -5 , 0, 5, and $10\text{ }^{\circ}\text{C}$ with positive and negative readout gradients applied along the axis of the cylindrical phantom (y direction). To examine the effects of temperature on homogeneity, images were acquired at 10, 5, and $0\text{ }^{\circ}\text{C}$, without high-order shimming, and at $-5\text{ }^{\circ}\text{C}$, both without and with high-order shimming.

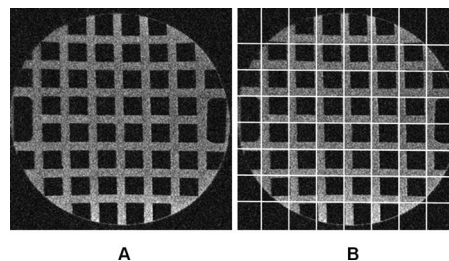


FIG. 4. (a) A 2D cross section selected from a 3D image data set of the phantom. Voxel size: $(100\text{ }\mu\text{m})^3$. (b) An equally spaced square grid superimposed on the cross section. A slight geometrical distortion is observed.

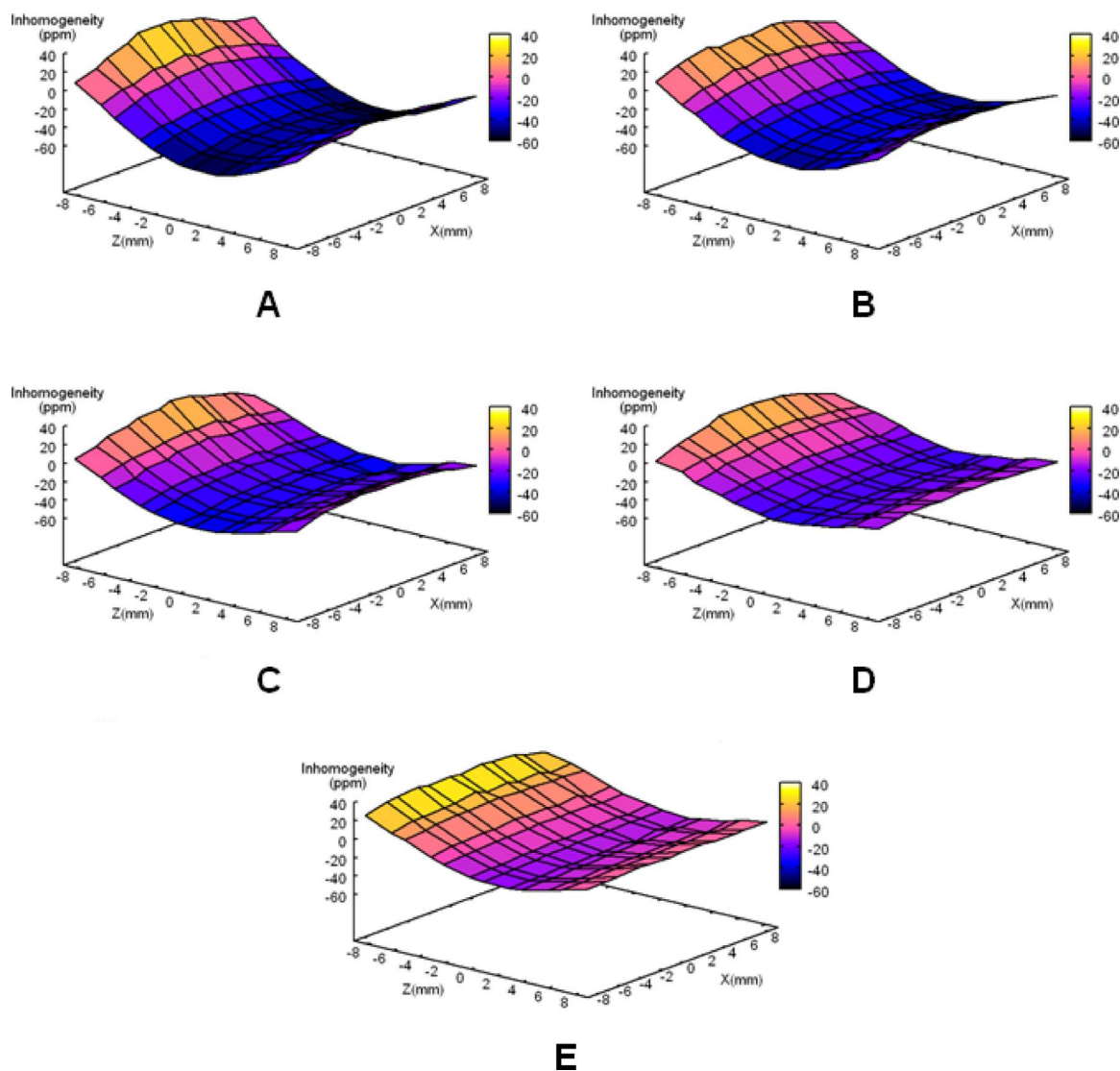


FIG. 5. (Color online) Magnetic field distribution in the xz plane. The field strength is expressed as the difference from the central field in ppm. The xz plane is located 9.4 mm away from the center of the magnet along the y direction. (a) -5 °C, shim current off. (b) 0 °C, shim current off. (c) 5 °C, shim current off. (d) 10 °C, shim current off. (e) -5 °C, shim current on.

The higher-order shim coil currents were determined using phase dispersion in two-dimensional (2D) echo-time shifted spin-echo images of a homogeneous cylindrical phantom (26 mm inner diameter, 50 mm in length) filled with dodecane. The current of each channel was adjusted through a try and error process to minimize the phase dispersion range in the phase image. This procedure was repeated for all shim coil channels until a suboptimum current combination was obtained.

The Cartesian coordinates of the vertex points visualized in the 3D image data sets of the phantom were collected using a homebuilt graphical user interface program developed using Visual C++ 2005 (Microsoft, Seattle, USA) and running under the MICROSOFT WINDOWS XP operating system. The calculation of the coordinates was based on the edge detection technique utilizing image derivative.¹⁸ The Larmor frequency shift from the central NMR frequency corresponding to the magnetic field inhomogeneity was calculated from the difference between the vertex point coordinates acquired with positive and negative readout gradients.¹⁹ The magnetic

field was calculated in the rectangular parallelepiped ($17 \times 17 \times 19$ mm³) region in the phantom.

For a demonstration of this system, 3D images of a snowpack sampled at Kitamura in Hokkaido prefecture in Japan were acquired using the same 3D imaging sequence as that used for the phantom. The snow sample was cylindrically cut and stored in a cylindrical container (24 mm inner diameter, 100 mm length), and filled with dodecane ($C_{12}H_{26}$; melting point: -13 °C) for MRI at -5 °C. During image acquisition, the gradient coils were cooled using several cooling fans to prevent heating the snow sample.

IV. RESULTS AND DISCUSSION

Figure 4 shows an axial cross section selected from a 3D image data set of the phantom. Because the in-plane coordinate axes were phase encoding directions (x and z directions), image distortion in this plane was caused by gradient field nonlinearity. Although quantification of the linearity of

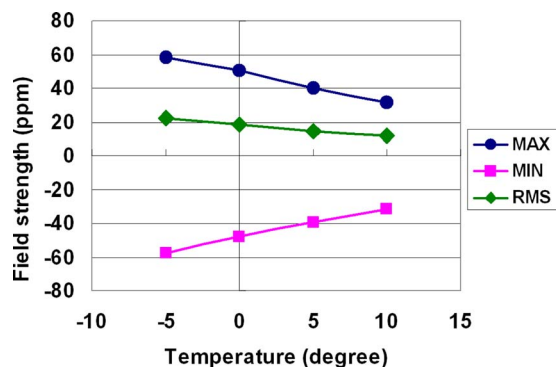


FIG. 6. (Color online) Temperature dependence of the maximum, minimum, and rms values of the magnetic field measured in the $17 \times 17 \times 19$ mm³ rectangular parallelepiped region. The field strength is expressed as the difference from the central field in ppm.

the gradients has not been performed, we think that this image demonstrates good linearity of the x - and z -gradient coils, as shown in Fig. 4(b).

Figure 5 shows the magnetic field distribution in the xz plane, 9.4 mm away from the center of the magnet along the y direction. Figures 5(a)–5(d) show the magnetic field distribution measured at -5 , 0, 5, and 10 °C without shim coil currents. These graphs clearly show that the magnetic field homogeneity increases with increasing temperature. Figure 5(e) shows the magnetic field distribution at -5.0 °C with shim coil currents, which were adjusted using phase images of echo-time shifted 2D spin-echo images. This figure clearly shows that the magnetic field homogeneity was dramatically improved by the shim coil.

Figure 6 shows temperature variation of the maximum, minimum, root-mean-square (rms) values of the magnetic field strength measured in the rectangular parallelepiped region. This graph clearly shows that the inhomogeneity (the difference between the minimum and maximum values of the magnetic field) approaches zero at about 25 °C, where the magnet shimming was performed in the factory. When the higher-order shim coil current was turned on at -5 °C, the inhomogeneity was improved from 117 to 59 ppm. The 59 ppm value was about ± 3 pixel shift in the present pulse sequence. This result shows that geometric distortion caused by the magnetic field inhomogeneity is less than three pixels. Therefore, the geometric distortion caused by the pixel shift would be improved for geometrical quantification of the MR images.²⁰

Figure 7 shows 2D cross sections selected from a 3D image data set of the snowpack acquired at -5 °C. These cross-sectional images clearly visualize the boundary between the compact and granular snow and their 3D structure. These images also demonstrate that there is little sample heating effect by the gradient coils during the 16 h measurement time.

Our group has performed 3D MR microscopic imaging of snow using a 4.7 T vertical bore superconducting magnet since 2000.^{21,22} This MRI system had several disadvantages for snow study mainly because the MRI system was installed

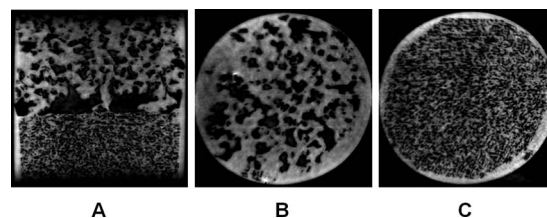


FIG. 7. 2D cross sections selected from a 3D image data set of a snowpack. The upper and lower parts are granular and compact snow, respectively. (a) Vertical plane. (b) Horizontal plane in the upper part. (c) Horizontal plane in the lower part.

at normal (20–25 °C) room temperature. The compact MRI system developed in this study solved most problems of the superconducting MRI system we have used.

In conclusion, we have developed a compact MRI system for a cold room and demonstrated its usefulness by acquiring 3D MR microscopic images of a snowpack. Other applications, such as the visualization of living tissue, plants, and insects below freezing point will be expected.

ACKNOWLEDGMENTS

We acknowledge Mr. Shunichi Nakatsubo at Hokkaido University for his technical contribution to this research.

- 1 T. Haishi, M. Aoki, and E. Sugiyama, *Proc. Intl. Soc. Mag. Reson. Med.* **13**, 869 (2005).
- 2 B. Beck, D. H. Plant, S. C. Grant, P. E. Thelwall, X. Silver, T. H. Mareci, H. Benveniste, M. Smith, C. Collins, S. Crozier, and S. J. Blackband, *Magn. Reson. Mater. Phys.* **13**, 152 (2002).
- 3 V. C. Behr, T. Weber, T. Neuberger, M. Vroemen, N. Weidner, U. Bogdahn, A. Haase, P. M. Jakob, and C. Faber, *Magn. Reson. Mater. Phys.* **17**, 353 (2004).
- 4 M. Weiger, D. Schmidig, S. Denoth, C. Massin, F. Vincent, M. Schenkel, and M. Fey, *Concepts Magn. Reson.* **33B**, 84 (2008).
- 5 NEOMAX magnet catalog: <http://www.hitachi-metals.co.jp/prod/prod03/pdf/hg-a22.pdf>.
- 6 T. Haishi, T. Uematsu, Y. Matsuda, and K. Kose, *Magn. Reson. Imaging* **19**, 875 (2001).
- 7 K. Halbach, *Nucl. Instrum. Methods* **169**, 1 (1980).
- 8 H. Zijlstra, *Philips J. Res.* **40**, 259 (1985).
- 9 H. A. Leupold, E. Potenziani II, and M. G. Abele, *J. Appl. Phys.* **64**, 5994 (1988).
- 10 M. Aoki and T. Tsuzaki, US Patent No. 7,084,633 (2006).
- 11 M. Sagawa, S. Fujimura, N. Togawa, H. Yamamoto, and Y. Matsuura, *J. Appl. Phys.* **55**, 2083 (1984).
- 12 T. Miyamoto, H. Sakurai, H. Takabayashi, and M. Aoki, *IEEE Trans. Magn.* **25**, 3907 (1989).
- 13 W. A. Anderson, *Rev. Sci. Instrum.* **32**, 241 (1961).
- 14 R. Turner, *J. Phys. D: Appl. Phys.* **19**, L147 (1986).
- 15 J. Jianming, *Electromagnetic Analysis and Design in Magnetic Resonance Imaging* (CRC, Boca Raton, FL, 1998).
- 16 D. E. Goldberg, *Genetic Algorithms in Search, Optimization and Machine Learning* (Addison-Wesley, Boston, 1989).
- 17 K. Kose, in *NMR Imaging in Chemical Engineering*, edited by S. Stapf and S.-I. Han (Wiley, New York, 2006), p. 77.
- 18 D. Wang, D. M. Doddrell, and G. Cowin, *Magn. Reson. Imaging* **22**, 529 (2004).
- 19 A. Kawanaka and M. Takagi, *J. Phys. E* **19**, 871 (1986).
- 20 D. Wang, W. Strugnell, G. Cowin, D. M. Doddrell, and R. Slaughter, *Magn. Reson. Imaging* **22**, 1211 (2004).
- 21 T. Ozeki, K. Kose, T. Haishi, S. Hashimoto, S. Nakatsubo, and K. Nishimura, *Magn. Reson. Imaging* **21**, 351 (2003).
- 22 T. Ozeki, K. Kose, T. Haishi, S. Nakatsubo, and Y. Matsuda, *Magn. Reson. Imaging* **23**, 333 (2005).